Journal of Materials Chemistry A

A Dramatic Reduction in the Sintering Temperature of the Refractory Sodium β''-Alumina Solid Electrolyte via Cold Sintering

Journal:	*Journal of Materials Chemistry A*
Manuscript ID	TA-ART-07-2021-005933.R1
Article Type:	Paper
Date Submitted by the Author:	28-Aug-2021
Complete List of Authors:	Grady, Zane; Pennsylvania State University, Materials Science and Engineering; Materials Research Institute Ndayishimiye, Arnaud; Pennsylvania State University, Materials Research Institute Randall, Clive; The Pennsylvania State University, Materials Science and Engineering; Penn State Materials Research Institute, Materials Research Institute

A Dramatic Reduction in the Sintering Temperature of the Refractory Sodium β''-Alumina Solid Electrolyte via Cold Sintering

Zane Grady*[,1,2] , Arnaud Ndayishimiye[2], Clive Randall[1,2]

[1]Materials Science and Engineering Department, The Pennsylvania State University, University Park, PA, 16802

[2]Materials Research Institute, Millennium Science Complex, University Park, PA, 16802

*Corresponding author: zmg19@psu.edu, tel: (401)741-3432

1. Abstract

The cold sintering process is successfully applied to one of the most refractory solid-state sodium-ion electrolytes, namely sodium beta alumina (SBA). By using a hydroxide-based transient solvent, SBA is densified below 400°C, whereas conventional solid-state sintering is known to require sintering temperatures around 1600°C. This dramatic reduction in sintering temperature (ca. T_{sinter} ~ 20% of T_m) is achieved by cold sintering with the addition of 10 wt.% solid NaOH transient phase, 360 MPa of uniaxial pressure, heating to 350-375°C, for a dwell time of three hours. The resulting pellets exceed 90% of the theoretical density for SBA and exhibit ionic conductivities of ~10^{-2} S.cm^{-1} at 300°C, as measured by electrochemical impedance spectroscopy. The structural changes occurring during cold sintering are reversed with an intermediate temperature annealing step (ca. 1000°C) which improves the ionic conductivity. This study therefore highlights the opportunities and remaining challenges in applying cold sintering to refractory, air-sensitive, electroceramics.

Keywords: cold sintering, solid electrolyte, beta alumina

2. Introduction

Sodium β''-alumina (SBA) is one of the few commercialized solid-state alkali ion electrolytes, despite decades of research conducted on such materials. The SBA electrolytes have been successfully integrated into high temperature secondary batteries with liquid electrodes, the chemistries of which include Na|S and Na|NiCl (also referred to as "ZEBRA" batteries).[1] SBA is well-suited for these applications owing to its excellent stability under such conditions while maintaining high ionic conductivity at elevated temperatures, in contrast to other well-studied solid-state sodium ion electrolytes, such as NASICON-structured $Na_3Zr_2Si_2PO_{12}$, which tend to be unstable at higher temperatures and in contact with alkali metals.[2], [3] The coupling of high temperature stability and highly anisotropic ionic conductivity are a consequence of the SBA structure; the mobile sodium ions are confined within conductive basal planes, separated from one another by strongly bonded layers of refractory spinel-Al_2O_3.[4], [5] The ionic conductivity in the other principle directions of the structure is effectively negligible, thereby there has to be complex tortuous pathways with the microstructure of β''-Al_2O_3.[6]

These strongly bonded alumina layers are responsible for the excellent thermal and chemical stability of the sintered bulk ceramics, but they also require unusually high sintering temperatures (typically $\geq$ 1600°C) in order for the densification process to proceed.[7] These notably high sintering temperatures introduce a number of issues in the processing of SBA, including but not limited to: (1) loss of sodium due to volatilization, (2) thermally induced phase transformation from the β''-phase to the less conductive β'-phase (SBA')[8]–[10], and (3) abnormal/excessive grain growth during prolonged dwell times at peak sintering temperatures, resulting in poor mechanical properties in the final polycrystalline ceramics[11]. SBA thus illustrates an unfortunately common dichotomy in solid-state ionic conductors; their structures are

characterized by both light, mobile, ions (e.g. Li^+, Na^+) and a strongly bonded, rigid, framework (e.g. spinel Al_2O_3), such that the high sintering temperatures required by the latter result in a loss of control over the former.[12], [13] For these reasons, it is of great interest to the ceramics community to reduce the peak sintering temperature of electroceramics, even if the synthesis/calcination temperature of the powder remains relatively high.

The issues associated with conventional high temperature sintering of SBA have been known for many decades.[3], [14] The undesired SBA to SBA' phase transformation can be mitigated by stabilizing the SBA phase *via* doping with Li_2O or MgO, but this introduces processing and structural complexities.[8], [9], [15] Aliovalent doping and sodium loss can be avoided by substituting the solid-state reaction synthesis process with a vapor-phase synthesis process, where a composite of yttria-stabilized zirconia (YSZ) and α-Al_2O_3 is first synthesized and sintered (ca. 1600°C) followed by post-sintering calcination of the sintered ceramic in the presence of a sodium source, resulting in the formation of a β''-alumina/YSZ composite.[16], [17] These composites are highly conductive and strong but contain a large volume fraction (ca. 30 vol.%) of non-conductive YSZ which is required for oxygen diffusion during the conversion reaction.

Alternatively, the sintering process itself can be modified to promote sintering at lower temperatures. Liquid phase sintering utilizing sintering additives such as TiO_2 have been shown to lower the sintering temperature to 1400°C, while retaining relatively high conductivity in the fine-grained SBA.[7], [18]–[20] Hot pressing has also been shown to reduce the sintering temperature of SBA to 1100°C, but the process very intensive and the varies in effectiveness.[21]–[23] Most recently, field-assisted sintering techniques such as Spark Plasma Sintering (SPS) have been shown to lower the sintering temperature of SBA to 1300°C while also offering a high degree of control over the orientation of the grains within the polycrystalline ceramic.[24]–[26] Microwave-

assisted sintering has also been recently applied to SBA[27], [28]. These techniques all exploit unique combinations of driving forces for sintering (e.g., applied pressure, capillarity) and demonstrate unique advantages, however none of these techniques has been shown effective in achieving any degree of densification below 1100°C.

Cold sintering is an emerging alternative sintering technique which involves the mixing of the parent phase, SBA in this case, and a secondary transient phase. The powder mixture is then simultaneously pressed and heated above the melting or boiling point of the transient phase, which is thought to drive dissolution at particle contacts and subsequent precipitation at newly formed grain boundaries.[29]–[31] The combination of these multiple driving forces (temperature, pressure, chemical reactivity) has been shown to reduce the sintering temperature of a gamut of ceramics from the conventional solid-state sintering regime (ca. 70% of T_m) to only hundreds of degrees Celsius (ca. 25% of T_m)[32], [33]. This technique has been of particular interest for ceramic ion conductors given the previously described sintering dichotomy and the desire to co-process electrochemical ceramics with other, thermally fragile, conductive additives.[12], [34]–[36] Furthermore, large reductions in sintering temperature have the potential to significantly reduce the energy used during sintering and expedite decarbonization process of the ceramics industry.[37]

We recently applied cold sintering to the NASICON-type solid-state sodium ion electrolyte, $Na_3Zr_2Si_2PO_{12}$, demonstrating that the sintering temperature of the ceramic could be reduced from over 1200°C to under 400°C when a solid hydroxide transient phase was used.[38] The sodium hydroxide (NaOH) solid hydroxide transient phase was introduced as a powdered salt and proved much more effective in promoting cold sintering relative to cold sintering driven by a concentrated solution of NaOH and H_2O.[31], [39], [40] In this work, we sought to extend this

approach to an even more refractory solid-electrolyte, SBA. Prior to this work, cold sintered ionic conductors have usually required conductive additives, such as salts or polymers, to improve the ionic conductivity.[41], [42]

3. Experimental

Materials

Mg-stabilized SBA having an approximate composition of $Na_{1+x}(Mg_xAl_{11-x})O_{17}$ (x = 0.51, estimated from electron dispersive spectroscopy) was purchased from MSE Supplies. Sodium hydroxide powder (97% purity) was purchased from Sigma Aldrich. All powders were stored under vacuum at 80°C when not in use.

Sintering

Cold sintering with a hydroxide transient solvent was described previously.[38], [39], [43] Briefly, the NaOH and SBA were weighed and mixed by hand in a fume hood. The powder mixture was then loaded into a stainless-steel die (inner diameter of 13 mm) with nickel foil (99%, Alfa Aesar) separators between the powder and the punch faces. The die was then inserted into a band heater, affixed with a thermocouple, and loaded into a carver press equipped with heated platens and with the temperature and pressure applied simultaneously. Once the dwell time was complete, the temperature controller was switched off and the pressure was released naturally with cooling. The pellets were then removed and stored under vacuum. An extended description of the cold sintering process and an *in-situ* densification profile as a function of time is provide in the supporting information (**Figure S1-S2**).

Characterization

The SBA pellets were mechanically polished with silicon carbide grinding paper after sintering or before heat treatment prior to any characterizations. The density of the pellets was assessed both geometrically (*via* volume and mass measurements) and with Archimedes method using ethanol as a solvent. For pellets above 90% relative density, both methods agreed well (i.e., ±3% agreement). Pellet dimensions were typically 0.7 to 1.0 mm in thickness and 13.0 mm in diameter.

X-Ray diffraction (PANalytical Empyrean, Cu Kα) was conducted on polished pellet surfaces in a Bragg-Brentano configuration with a tension of 45 kV, current of 40 mA, step size of 0.01°, and dwell time of 200s/step over a range of 5° to 70°. Pellets of cold sintered SBA were sputtered with ion-blocking platinum electrodes (Kurt J. Lesker, approximate area of 0.2 cm^2, 100 nm thick) with a Quorum Technologies sputter coater (EMS 150R-S) for electrical measurements. Electrochemical impedance spectroscopy (EIS, Modulab XM MTS) was taken from 1 MHz to 0.1 Hz with an AC amplitude of 10 mV. EIS was measured from room temperature to 350°C with a thermal soak time of 20 minutes per temperature. EIS fitting was conducted using ZView software (Scribner Associates). Scanning electron microscopy (SEM, FESEM Verios NanoSEM) was conducted on fracture surfaces of pellets coated with 6 nm of iridium with an accelerating voltage of 3kV. Transmission electron microscopy was carried out under cryogenic conditions using a Talos F200X (FEI) microscope equipped with a Gatan cryogenic holder in both dark field and scanning mode (STEM) at an accelerating voltage up to 200 kV. Chemical mapping was performed with a SuperEDX detector. The TEM samples were prepared by Ga^+ focused ion beam milling (Helios 660, FEI).

Fourier transform infrared (FTIR) spectra were collected using a Vertex 70 spectrometer (Bruker,MA, USA) equipped with a liquid nitrogen-cooled narrow-band MCT detector and a

Harrick Praying Mantis™ Diffuse Reflectance Infrared Fourier Transform spectroscopy (DRIFTs) cell (Harrick Scientific Products, Inc., NY, USA). To minimize the impact of air exposure prior to DRIFTS experiments, β-Al_2O_3 samples were dried at 80 °C under vacuum, then moved into transportable vacuum boxes a few minutes before the measurement. Pieces of β''-Al_2O_3 pellets were grinded and mixed with spectroscopy grade anhydrous KBr (with a 3:97 mass ratio). The mixture was then carefully poured in a conical sample holder. Spectra were collected at room temperature and are an average of 100 scans in the 400-4000 cm^{-1} wavenumber range. The background correction was performed with the infrared signal of pure KBr. Afterwards, FTIR spectra were normalized and analyzed using the spectroscopy software OPUS.

Some pellets were subjected to a post-annealing process in a flowing argon atmosphere inside a tube furnace a various temperatures for three hours with a thermal ramp rate of 3°C and cooling rate of 1°C. Prior to annealing, the sample surfaces were polished such that the platinum electrodes could be applied immediately after removal from the furnace.

4. Results and Discussion

4.1 Structure and Microstructure of the cold sintered SBA

The cold sintering parameters from previous studies using similar flux systems was found to be effective in the case of SBA as well. These conditions were 10 wt.% (14.6 vol.%) of pure sodium hydroxide (NaOH) powder mixed into 90 w% (85.4 vol.%) of the parent SBA powder, which was then pressed at 360 MPa and heated to 375°C and held for three hours. The relative density was found to be constant for 8 wt.% to 12 wt.% NaOH, while weight fractions of NaOH outside of this range resulted in poor densification. All powders were stored under vacuum and in the presence of desiccant to minimize moisture absorption from the atmosphere. With these conditions,

densities of 3.04 ± 0.09 g/cm^3 (92.7 ± 2.70 %) were reproducibly achieved. The mutual effectiveness of these conditions on such dissimilar materials (SBA and $Na_3Zr_2Si_2PO_{12}$) is likely due to both the reduced propensity for incongruent leeching of sodium during sintering, as well as the increased solubility of oxides under pressurized molten hydroxide conditions.[44]–[46]

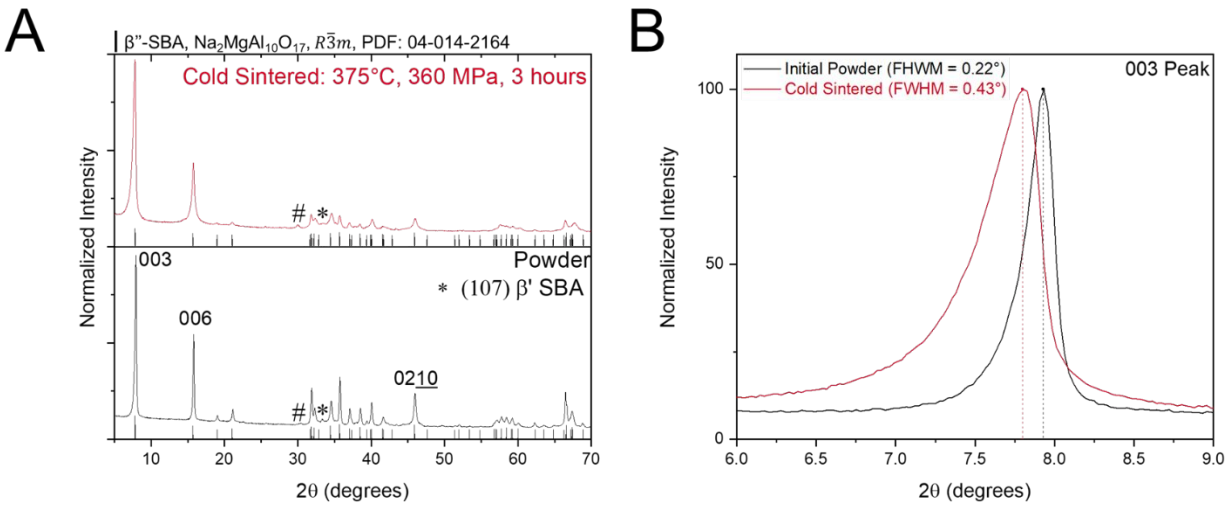

Figure 1 An XRD spectra of the initial SBA powder and a cold sintered pellet (**A**). The XRD spectra of the characteristic 003 reflection of the conduction plane for SBA (**B**). (∗) denotes the β' SBA phase. (#) denotes a secondary, unidentified impurity. FWHM = Full Width Half Maxima. Reference β''-SBA structure: PDF 04-014-2164[4]

X-ray diffraction (XRD) was performed on a representative cold sintered pellet (10 wt.% NaOH, 375°C, 360 MPa, 3 hours) to assess the phase purity. **Figure 1A** depicts a typical XRD pattern of such a pellet alongside an XRD spectra for the initial powder. The powder is primarily comprised of the highly conducting β'' phase (SBA, rhombohedral, $R\bar{3}m$) and a small amount of the less-conductive β' phase (SBA', hexagonal, $P6_3/mmc$), the latter deduced from the small peak at 33.5°. Previous studies have estimated the relative amount of SBA versus SBA' by comparing the height of characteristic peaks for each phase[7], but it should be noted that the results can vary

based on the SBA stabilizing dopant, specific peak couple selected, and reference structure chosen. In the present case, the intensity of the $(02\overline{1}0)$ β'' reflection ($I_{\beta''}$) is compared to that of the (107) β' reflection ($I_{\beta'}$) with the equation,

$$f(\beta'')\% = \left(1 - \frac{I_{\beta'}}{I_{\beta''}}\right) * 100\%$$

From this estimation, the powder is comprised of about 90% of the β'' phase. Besides this sizable fraction of β', all other XRD peaks can be indexed with the $R\overline{3}m$ β'' SBA phase (PDF 04-014-2164).[4], [5]

The full XRD spectra of the cold sintered pellet is very similar to that of the initial powder (**Figure 1A**). The primary conduction layer peaks ((003), (006)), are broader and slightly shifted relative to the powder spectra. A decrease in peak sharpness, especially at the high angles, could indicate some loss of long-range order but could also be due to the reduced intensity arising from the spectra of a polished pellet compared to fine powder. The only additional peak which cannot be indexed to the β'' phase is at approximately 29.0° 2Θ (marked '#' in **Figure 1A**) which is presently unidentified. This peak is also present in the initial powder, albeit with very low intensity, suggesting that this phase is not primarily generated during the cold sintering process.

Interestingly, the (107) β' peak is not as prominent in the XRD spectra of the cold sintered pellet relative to the initial powder. The background of the cold sintered XRD pattern is higher (normalized to 003-peak height) relative to the powder, so the SBA' phase may lie below the detection limit. However, this result does indicate that very little, if any, SBA' is generated during the cold sintering process.[15] Additional details regarding the phases present in the samples are given with XRD refinements in the supporting information (**Figure S1**).

Finally, we note two other aspects of the XRD spectra which suggest a water absorption and carbonate formation during cold sintering. First, the primary conduction plane peak (003, **Figure 1B**) is shifted by 0.13° 2θ, indicating an expansion of about 1.6%. Second, we note that the broadening of the (003) peak (full-width-half-maxima increases by 0.21°) is unevenly distributed, i.e. the peak broadens asymmetrically after cold sintering. The conduction plane expansion is consistent with the intercalation of water molecules[47], which displaces sodium ions to the surface of the ceramic, resulting in the simultaneous formation of Na_2CO_3[8], [48]–[50]. These reactions are known to proceed readily upon exposure to air, so the procession of the reaction during cold sintering (in ambient atmosphere) is unsurprising. It is worth noting that the conventional solid-state sintering process of SBA requires temperatures greater than 1400°C, which is more than sufficient to decompose Na_2CO_3 and expel any intercalated water. Thus, while cold sintering dramatically reduces the sintering temperature, the cold sintering temperature is insufficient to remove the carbonates/water molecules. An intermediate temperature annealing step is therefore required, as will be shown later in this article.

Microstructure of initial powder and as-cold sintered pellets

Scanning electron microscopy (SEM) was performed to confirm the density measurements. The initial powder (**Figure 2A**) exhibits the characteristic platelet morphology of the layered SBA. The particle size ranges from about 1 to 5 μm. A representative image of a fracture surface from a cold sintered pellet is shown in **Figure 2B**.The lack of any significant porosity in the bulk microstructure is a clear confirmation of the high relative density.

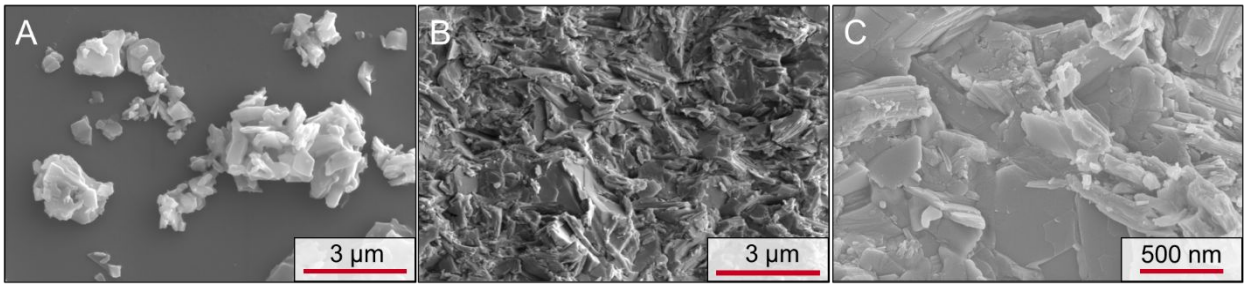

Figure 2 An SEM image of the initial SBA powder (**A**), a representative area of a cold sintered fracture surface (**B**), and a magnified image of well-sintered grains within the cold sintered pellet (**C**).

Higher magnifications of the cold sintered microstructure (**Figure 2C**) illustrate the formation of well-sintered grain boundaries within the cold sintered SBA ceramic. The individual grains retain the hexagonal platelet crystal habit of the initial powder. The sintered grains are approximately the same dimensions as the original powder, implying a lack of grain growth during the cold sintering of SBA. Well-faceted grain boundaries can clearly be observed at high magnifications (**Figure 2C**), indicating that a sintering process has occurred. Collectively, these observations prove that cold sintering can be applied to SBA to produce dense microstructures which retain the grain size of the initial powder, thus avoiding the exaggerated grain growth phenomena frequently observed in conventional sintering processes. Elemental mapping (**Figure S4**) provides direct evidence for the presence of sodium carbonates on the surface of the as-cold-sintered SBA samples. Finally, we note that the applied uniaxial pressure appears to induce some microstructural texturing perpendicular to the direction of applied pressure (Lotgering analysis, **Figure S5**). Texturing has been previously observed in spark plasma sintered SBA[26], albeit to a much higher degree, which resulted in the conductivity of the sample becoming magnified by a factor of about 2.5. However, this effect should be small relative to other factors such as secondary phases and relative density in the cold sintered SBA samples.

To investigate the microstructure of the as-cold-sintered in more detail, cryogenic transmission electron microscopy was performed (**Figure 3**). It should be noted that fast ionic conductors such as SBA are difficult to probe with transmission electron microscopy due to beam degradation when cryogenic conditions are not employed. In **Figure 3A-B**, the dense microstructure of the cold sintered beta alumina can be clearly observed. Despite the high aspect ratio of the SBA crystal habit (elongated platelet), few pores are present in the microstructure owing to the grain rearrangement and grain boundary formation during cold sintering. Moreover, certain regions appear to contain grains which exhibit texturing in the form of the platelet-shaped grains stacking upon one another with aligned *c*-axes (**Figure 3B**). This is consistent with the aforementioned Lotgering analysis (**Figure S5**).

Closer inspection of the TEM micrographs sheds light on the grain boundary regions (**Figure 3C-D**). The grain boundary regions in the cold sintered SBA are generally amorphous and span distances on the order of 10 to 20 nanometers. Chemical mapping of the grain boundary regions (**Figure S4**) confirms their chemical similarity to the adjacent crystalline grains, suggesting that the amorphous grain boundary regions are the result of the dissolution-precipitation process driven by cold sintering. The amorphous regions fill the irregularly shaped intergranular spaces which explains how relative densities of >90% are obtained without significant grain growth for a microstructure of platelet-shaped SBA grains, which cannot pack efficiently compared to isotropic grains. Upon annealing (**Section 4.2**), these amorphous regions likely crystallize into similarly high-aspect ratio grains and evolve porosity in the process owing to the packing limitations imposed by the irregular grain morphology. Finally, we also note some evidence of a terrace-ledge structure at the edges of some grains adjacent to intergranular amorphous regions (**Figure 3D**), which may suggest that the dissolution-precipitation process

during cold sintering occurs preferentially along certain crystallographic directions, such as the edges of the platelets (e.g.,$(01\bar{1}0)$) compared to the basal plane (003).

The relationship between the ionic conductivity and grain/grain-boundary structure in SBA has been a subject of debate for many decades.[51] Numerous authors have proposed contrasting microstructural models to account for the anisotropic conduction properties of conventionally fired SBA, which account for abnormal microstructural factors by introducing concepts such as “easy” conduction paths through grains of varying levels of misorientation, among other effects.[6] For the purposes of this paper, it is sufficient to acknowledge that the inherent complexity of a polycrystalline arrangement of an anisotropic ion conducting ceramic can only be magnified by the contributions from the complexity in grain boundary regions noted in the previous paragraphs. These grain boundary regions in cold sintered SBA reflect the non-equilibrium nature of the low temperature sintering process compared to conventional sintering, which, owing to the high sintering temperature, produce microstructures much closer to the thermodynamic equilibrium state.

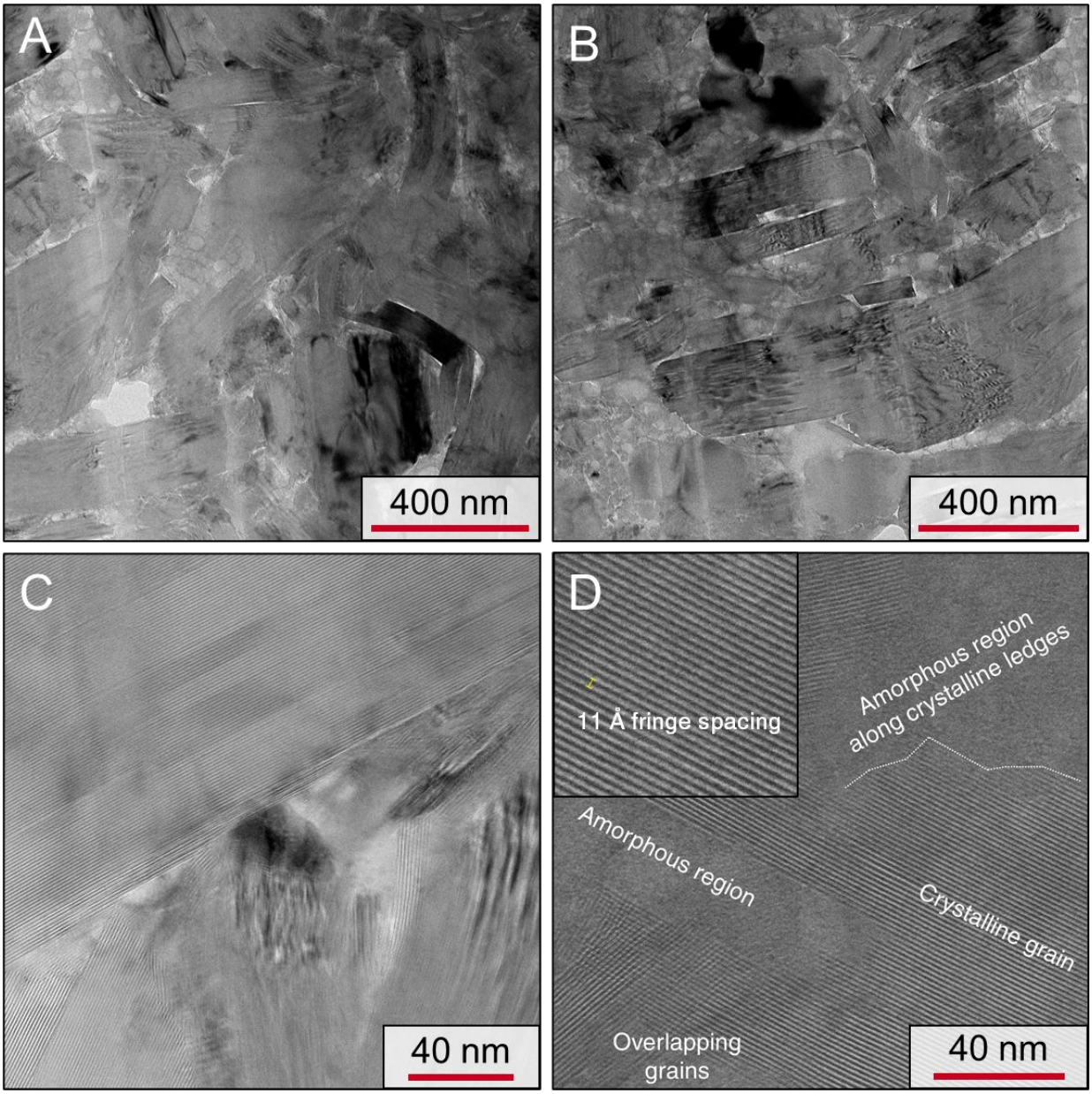

Figure 3 Transmission electron microscopy of as-cold-sintered SBA. Low magnification images depict a dense microstructure (**A**) with some texturing throughout the overall microstructure (**B**). High magnification images illustrate crystalline-amorphous interfacial regions at grain boundaries (**C-D**). Inset of (**D**) is magnified by 4 × to highlight fringe spacing. Dotted line in (**D**) outlines terrace-ledge crystalline-amorphous interface character.

Electrical properties of As-Cold-Sintered SBA

The ionic conductivity of the cold sintered SBA pellets was then measured with electrochemical impedance spectroscopy (EIS). When plotted in the complex plane (*Z'* versus *Z''*), a partial semicircle followed by a low frequency linear electrode response is observed, which is characteristic of polycrystalline ionic conductors with blocking electrodes.[52] From such complex plane plots, it is possible to calculate the frequency-independent resistance from extrapolation of the linear electrode response to the *Z'* axis intercept, as indicated in **Figure 4A**. This total resistance, denoted R_t, can then be used to calculate the total conductivity, σ_t,

$$\sigma_t = \frac{t}{R_t * A}$$

Where *t* and *A* are the sample thickness and electrode area, respectively. In this way, it is found that the cold sintered SBA samples typically have room temperature conductivities of around $3.4 * 10^{-7}$ S.cm^{-1}. Conventionally sintered polycrystalline Mg-stabilized SBA typically has room temperature conductivity values on the order of 10^{-3} S.cm^{-1}. The high resistance of the cold sintered SBA at room temperature is likely due to the non-conductive Na_2CO_3 and intercalated water noted in the previous section. This room temperature conductivity is improved upon by further annealing, as will be shown in the next section. The shape of the semicircle is somewhat asymmetric and thus is fit with a Havriliak-Negami element[53]–[55], the fitting parameters of which are given in the supporting information (**Figure S6-S7**, **Table S1-2**).

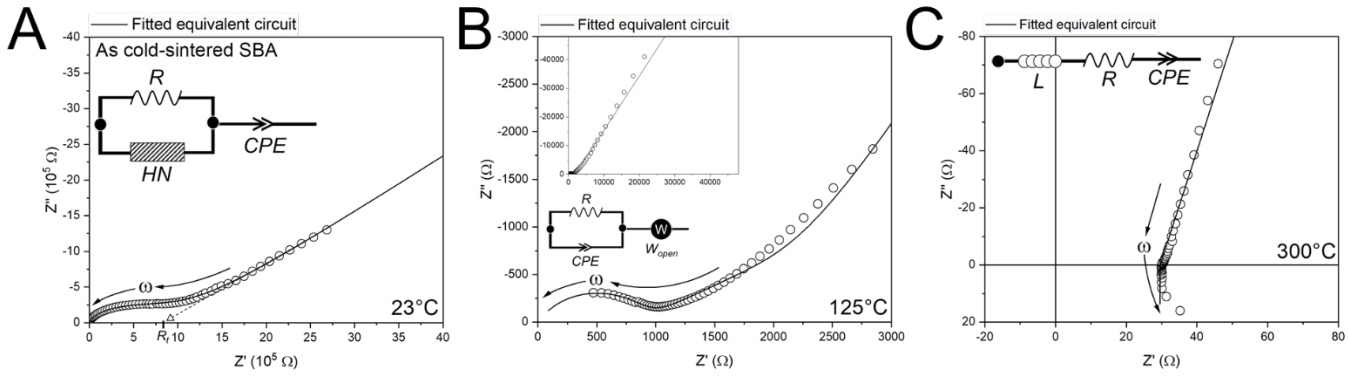

Figure 4 The EIS response of as-cold-sintered SBA is depicted at room temperature (**A**), 125°C (**B**), and 300°C (**C**). Each spectrum is fit with an appropriate equivalent circuit (insets), the fitting parameters of which are given in the supporting information. Angular frequency $(\omega) = 2\pi f$. Abbreviations: *R*: Resistor, *HN:* Havriliak-Nagami element, *CPE:* Constant-phase element, W_{open}*:* Warburg (open-circuit), and *L:* inductor.

As the temperature is increased, the impedance of the samples decreases quickly (**Figure 4B**). The shape of the semicircle formed in the complex plane also changes from asymmetric at low temperatures (**Figure 4A**) to a suppressed symmetrical semicircle at 150°C (**Figure 4B**). The impedance spectra at 125°C is fit with a common equivalent circuit (**Figure 4B**, inset) in which a resistor and constant phase element (CPE) are placed in parallel to capture the grain boundary response, followed in series by a linear CPE to capture the electrode polarization. [52], [56]. Following the same procedure described in the previous paragraph, the total conductivity is at 125°C for the cold sintered SBA is $1.07 * 10^{-4}$ S.cm^{-1}.

At 300°C (**Figure 4C**), the impedance spectrum is characterized simply by a straight line from the electrode, with some inductance at the highest frequencies. The inductance is likely due to contributions from the electrode and silver wires in addition to some closed porosity which has been previously observed in conventionally sintered SBA[57], [58]. Taking R_t to be the high

frequency intercept with the *Z'* axis, the conductivity of the as-cold sintered SBA at 300°C is found to be $7.6 * 10^{-3}$ S.cm^{-1}.

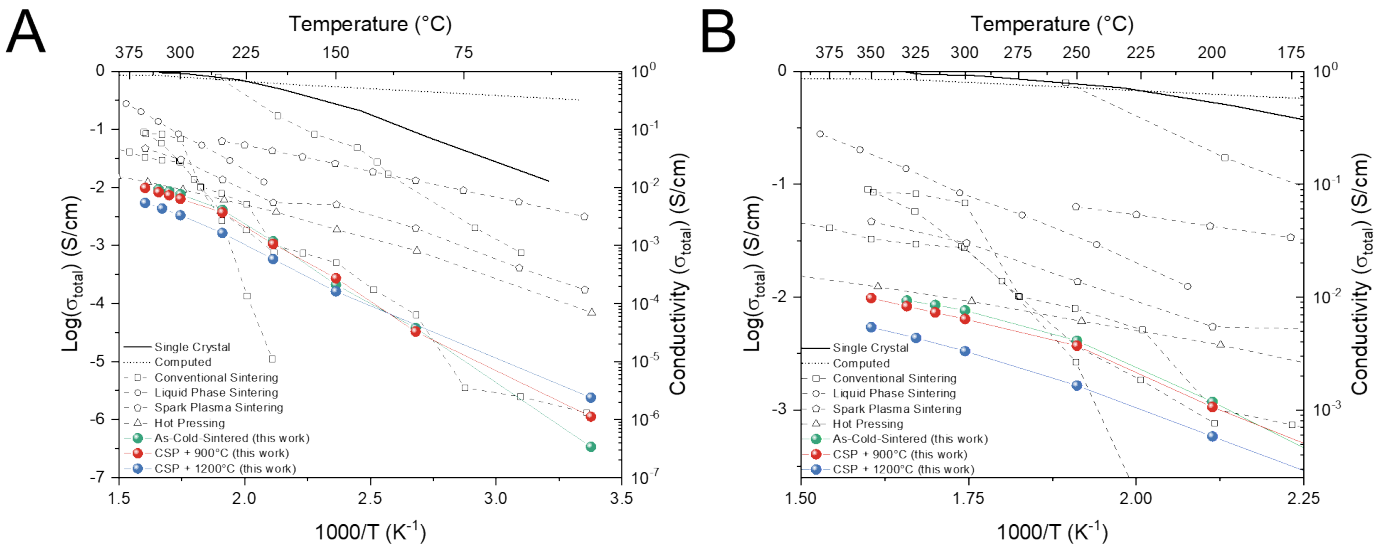

Figure 5 Conductivity as a function of inverse temperature for cold sintered and annealed samples is plotted alongside a representative set of prior work (**A**). The high temperature region of (**A**) is magnified in (**B**). Data from the literature includes computationally calculated conductivity[59], single crystal measurements[60], conventionally sintered polycrystalline SBA[61]–[64], liquid phase sintered SBA[19], spark plasma sintered SBA[24], [26], and hot pressed SBA[22]. Explicit references given in supporting information **Figure S8** and **Table S3**. Lines connecting points are given to guide the eye. Note the change in activation from ca. 0.5 eV to 0.2 eV at ca. 250°C for numerous polycrystalline samples.

In **Figure 5**, the total conductivity versus inverse temperature is plotted alongside a collation of data from the literature. From this Arrhenius plotting, it is clear that high temperature ($T \geq 300$°C) conductivity of the cold sintered SBA ($7.6 * 10^{-3}$ S.cm^{-1}) is within the lower boundary of the range of total conductivity values reported for SBA requiring sintering temperatures more than 1000°C greater than the cold sintering temperature. At lower temperatures, (ca. $T < 200$°C) the conductivity of the cold sintered SBA is lower than most previous reports,

however, it should be noted that there is significantly more non-Arrhenius behavior and a wider range of reported conductivities for other processing methods within this lower temperature window.

The activation energy of at these lower temperatures (ca. 23°C to 250°C) is higher for the as-cold-sintered SBA (0.54 eV) than the conventionally sintered SBA (ca. 0.3 eV). However, at temperatures above 250°C, the activation energy of the cold sintered SBA changes to 0.20 eV, which is consistent with previous studies. This can be more easily seen by enlarging the high temperature portion of the Arrhenius plot (**Figure 5B**) and by comparing the electrical properties these cold sintered samples with a representative set of conventionally processed polycrystalline SBA (**Table 1**).

Table 1 A compilation of other studies relating to the sintering of SBA and the resulting properties. Abbreviations: CSP – Cold Sintering Process, CS – Conventional Sintering, LPS – Liquid Phase Sintering, SPS – Spark Plasma Sintering.

Reference	Method	Sintering Temperature (°C)	σ at 300°C ($S.cm^{-1}$)	σ at 23°C ($S.cm^{-1}$)	E_a for $T \geq 200$°C (eV)	Relative Density (%)	Comment
This work	CSP	375	7.6×10^{-3}	3.40×10^{-7}	0.22	92.7	
This work	CSP + 900°C	900	6.4×10^{-3}	1.12×10^{-6}	0.26	89.6	
This work	CSP + 1200°C	1200	3.2×10^{-3}	5.22×10^{-5}	0.31	83.8	
[59]	Computed	-	1.0×10^{0}	-	-	-	Interpolated
[60]	Single Crystal	-	3.5×10^{0}	-	0.03	-	Interpolated
[61]	CS	1550	2.8×10^{-2}	-	0.23	75	
[62]	CS	1620	8.0×10^{-2}	-	0.51	96	σ at 250°C
[63]	CS	1600	6.8×10^{-2}	1.32×10^{-6}	0.15	98.5	
[64]	CS	1600	2.8×10^{-2}	-	-	98.5	
[19]	LPS	1520	8.4×10^{-2}	-	0.15	98.2	1 mol% Sn
[24]	SPS	1300	3.0×10^{-2}	1.74×10^{-4}	0.38	96.4	
[26]	SPS	1400	6.3×10^{-2}	3.16×10^{-3}	0.17	98.9	σ at 250°C
[22]	Hot Pressing	1700	9.1×10^{-3}	6.96×10^{-5}	0.19	99	

4.2 Improved Electrical Properties of the Annealed SBA

The XRD spectra and electrical response of the as-cold-sintered SBA is similar to previous reports of SBA which has intercalated water or generated carbonates [48], [49]. Prior work has shown that the water and carbonates can be removed with annealing under inert atmospheres. Thus, the as-cold-sintered SBA was subjected to annealing under argon at 900°C or 1200°C to investigate the possibility of removing said impurities from the cold sintered samples.

After annealing, the room temperature conductivity of the rises from $3.4 * 10^{-7}$ S.cm^{-1} (as-cold-sintered) to $1.1 * 10^{-6}$ S.cm^{-1} (900°C anneal) and $5.2 * 10^{-5}$ S.cm^{-1} (1200°C anneal). The activation energy below 200°C decreases from an initial value of 0.54 eV to 0.48 eV (900°C anneal) and 0.38 eV (1200°C anneal) (**Figure 5**). The conductivity at 300°C of the 900°C annealed sample remains close to the as-cold-sintered sample ($6.4 * 10^{-3}$ S.cm^{-1}) while the conductivity of the 1200°C annealed sample decreases to $3.2 * 10^{-3}$ S.cm^{-1}. This decrease in conductivity at 300°C as the annealing temperature is increased is likely due to de-densification during annealing[65]–[67], as suggested by micrographs shown in the next section. These changes impact the conductivity of the SBA through the removal of interfacial phases such as carbonates and hydroxyls along with some microstructural evolution.

The increased conductivity of the annealed samples is also exemplified by the impedance spectra at room temperature (**Figure 6**). After annealing, the large asymmetric semicircle is replaced by small, suppressed, semicircles at the highest frequencies followed by an electrode polarization. The impedance spectra of the annealed samples is best fit with two sets of parallel resistor/CPEs in series (**Figure S7**, **Table S2)**), suggesting two distinct responses. By noting that the second (lower frequency) semicircle increases in diameter while being held at room temperature, we ascribe the high frequency semicircle to the pure SBA response and the low

frequency semicircle to the re-formation of the Na_2CO_3, which was removed during annealing but forms quickly under ambient conditions. In light of this, the impedance measurements of the annealed samples were taken immediately upon removal from the furnace, thereby minimizing the carbonate contribution. The total conductivity remains derived from the extrapolation of the linear electrode response to the intersection of the *Z'* axis.

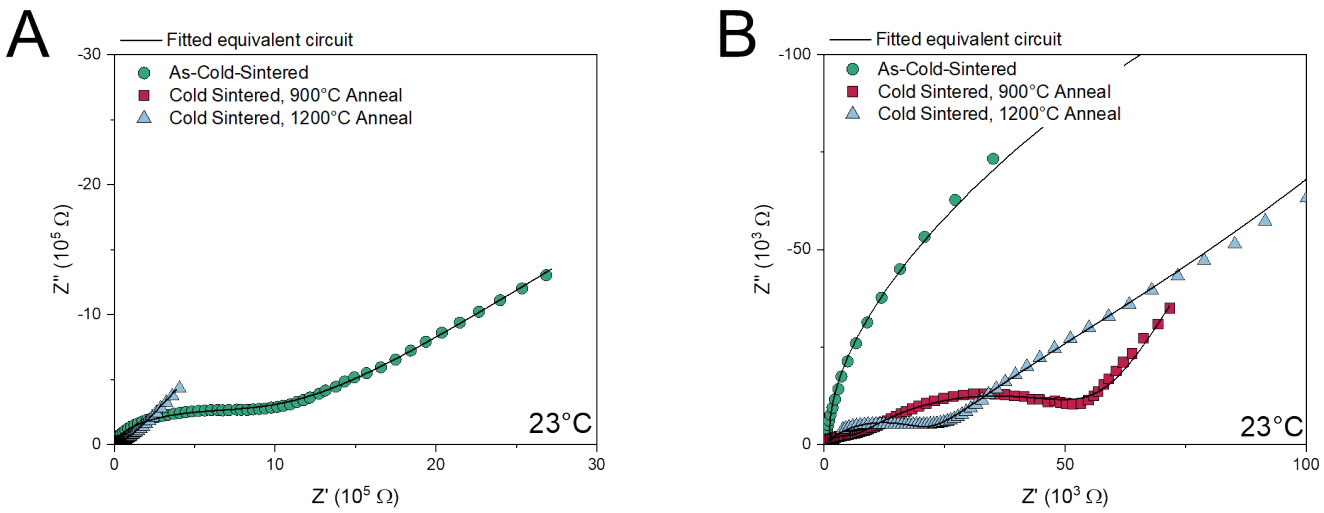

Figure 6 Room temperature EIS spectra of as-cold-sintered SBA compared to cold sintered SBA annealed at 900°C and 1200°C (**A**). A magnified view highlighting the more conductive annealed samples (**B**). Details regarding the equivalent circuits and fitting parameters are given in the supporting information (**Figure S3** and **Table S2**).

4.3 Changes in Microstructure and chemical bonding in the annealed SBA

The microstructure of the as-cold-sintered SBA is shown in **Figure 7A**, alongside that of samples which had been annealed under argon at 900°C (**Figure 7B**) and 1200°C (**Figure 7C**). As the annealing temperature is increased, the SBA grains grow, and it appears that some pores are formed/enlarged. This is especially evident in **Figure 7C** where the thickness of the SBA platelet-like grains is increased significantly relative to the powder (**Figure 2A**) and the as-cold-sintered samples (**Figure 2B-C**, **Figure 7A**). It is also clear that fair amount of enclosed porosity is evolved,

which is consistent with some progressively lower densities of the pellets as the annealing temperature is increased; the relative densities are 92.7%, 89.6%, and 83.8% for the as-cold-sintered, 900°C annealed, and 1200°C annealed samples respectively (**Table 1**). This decrease in relative density as the annealing temperature is raised is also consistent with the slightly lower ionic conductivity at high temperatures noted in the previous section.

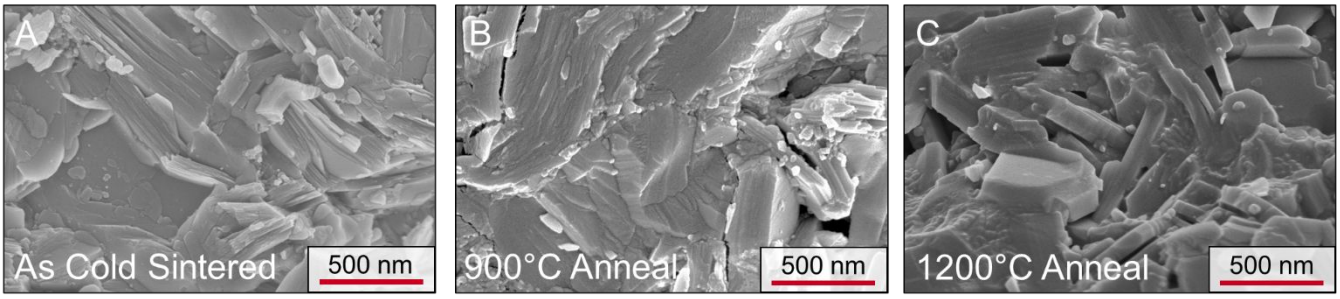

Figure 7 SEM images of the microstructure of an as-cold-sintered SBA sample (**A**) compared to that of a sample annealed at 900°C (**B**) and 1200°C (**C**)

XRD and FTIR were conducted on the initial powder, the as-cold-sintered samples, and the annealed samples to observe the removal of carbonates/moisture and changes in structure. **Figure 7A** illustrates the progressive peak sharpening as the samples are annealed, as well as a shift of the conduction layer peak (ca. 7.9° 2θ) to slightly lower angles, indicating a decrease in the conduction layer height and removal of water from the conduction plane. The annealed samples have (003) Bragg angles closer to that of the powder and small FWHM values which suggests a high degree of crystallinity; the Bragg angles (FWHM) are 7.93° (0.22°), 7.84° (0.43°), and 7.89° (0.17°) for the powder, as-cold-sintered pellet, and 1200°C annealed samples, respectively.

The expulsion of water and removal of carbonates is further evidenced by comparing the FTIR spectra of the powder, an as-cold-sintered sample, and an annealed sample (**Figure 7B**). IR bands characteristic of carbonates (1400 cm^{-1})[68], hydrated carbonates (1468 cm^{-1})[69], and water

(1630 cm^{-1})[70] are present in the the initial powder, which are then replaced by a single IR band at 1440 cm^{-1} in the cold sintered sample. This 1440 cm^{-1} band has been assigned to hydrated carbonates which form on SBA surfaces. After annealing, the intensity of the 1440 cm^{-1} decreases signficantly, indicating a removal of a superficial carbonate phase. Similarly, a broad band centered at 3301 cm^{-1} observed in the initial powder and the as-cold-sintered sample is replaced by two much smaller bands at 3483 cm^{-1} and 3088 cm^{-1} which points to a decrease in the amount of hydrogen-bonded hydroxyl groups[68], [71], similar to what one might expect from the removal of water from the conduction plane of the SBA.

These results collectively point to three factors which contribute to the increase in conductivity upon annealing of cold sintered SBA. First, the amorphous grain boundary regions observed in TEM (**Figure 3**) are recrystallized upon annealing as evidenced by the XRD peak sharpness and SEM images (**Figures 7-8**). Second, some grain boundaries in the as-cold-sintered SBA contain carbonates, which is coupled with water intercalation, and these features are removed by annealing, as evidenced by reduction in activation energy for conduction, (003) peak shifts, and FTIR signatures. Third, carbonates readily form at exposed SBA surfaces, as evidenced by the carbonate formation observed on the surface of a polished pellet (**Figure S4**) and the small signature in the FTIR (**Figure 8**). With respect to the third factor, it is expected that the annealing process produces a clean interface between the SBA pellets and the platinum electrode which is greatly improved relative to the as-cold-sintered pellet surfaces. While conventionally sintered SBA must contend chiefly with the third factor, our results demonstrate the additional factors which must be considered when processing such materials by new low temperature methods.

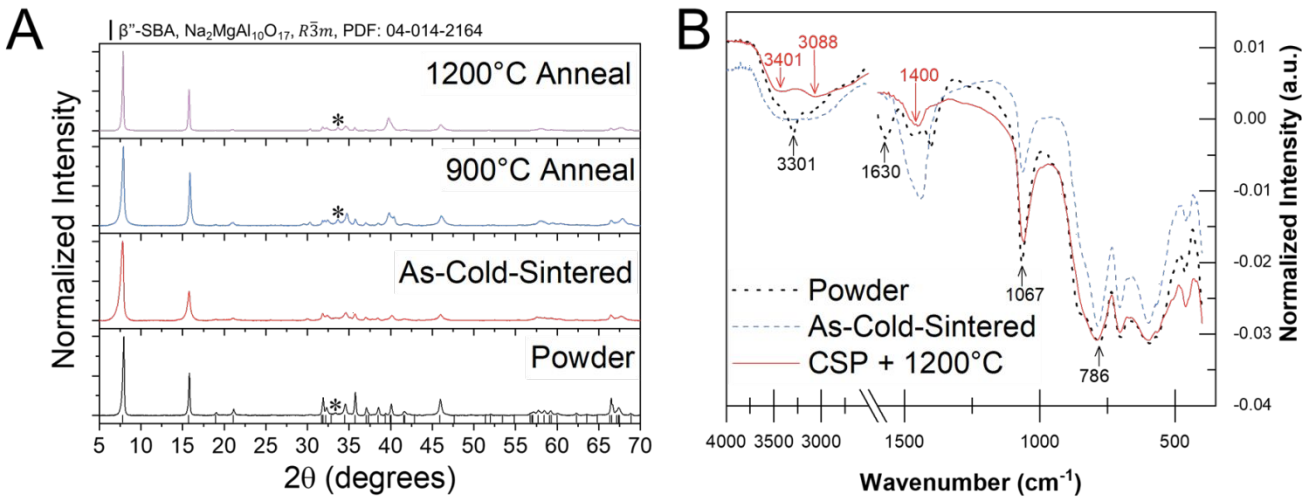

Figure 8 XRD Spectrum for the initial powder, the as-cold-sintered, 900°C, and 1200°C annealed SBA (**A**). The *β*' is marked with (∗). The FTIR spectra for the SBA powder, an as-cold-sintered sample, and a cold sintered sample annealed at 1200°C is also shown (**B**). CSP – Cold Sintering Process

4.5 Placing cold sintered SBA within the context of prior work

To summarize, we showed that the cold sintering process could be applied at 375°C with an NaOH transient phase to produce remarkably dense microstructures of *β*'' SBA. The electrical properties at high temperatures are competitive with conventionally fired SBA, but the low temperature conductivity and activation deviate from conventionally sintered SBA. The increased resistance at low temperatures appears to originate from the reaction of the SBA with water and carbon in the air. With intermediate temperature annealing, the absorbed water and carbonates are removed, and amorphous grain boundaries are crystallized, resulting in an improvement in low temperature conductivity.

The as-cold-sintered SBA may therefore be attractive for technologies which operate at high temperatures (ca. 300°C), such as sodium-metal-halide batteries, owing to the conductivity of the as-cold-sintered SBA being competitive with conventionally fired SBA at these temperatures. Furthermore, the energy savings associated with reducing the sintering

temperature[37] from 1600°C to 375°C may counterbalance the modest decrease in conductivity between samples sintered by conventional means and by cold sintering, respectively. However, for applications which require high conductivity at lower temperatures, the intermediate temperature annealing process appears to be necessary. While the annealing process improves the properties and aids in the study of the system as a whole, this secondary processing diminishes the amount of energy saved in sintering and opportunities to co-process SBA with very thermally fragile materials. Future work may investigate routes to apply a similar cold sintering process which does not require a post-annealing step.

To place these results within the context of the greater body of existing literature concerning the property-processing relationship of SBA, we have plotted the ionic conductivity at 300°C (**Figure 9A**) and relative density (**Figure 9B**) as a function of peak sintering temperature for this work and a large number of previous studies (22 studies over ~50 years). Examples of conventional sintering, hot pressing, liquid phase sintering, and field-assisted sintering all applied to polycrystalline SBA are represented in the set of literature references. Evidently, cold sintering accesses a unique processing window for this refractory solid electrolyte. A complete list of the references and associated data used to compile **Figure 9** is provided in the Supplemental Information (**Table S4**).[16], [18], [63], [64], [72]–[79], [19], [80], [81], [21]–[23], [26], [57], [61], [62]

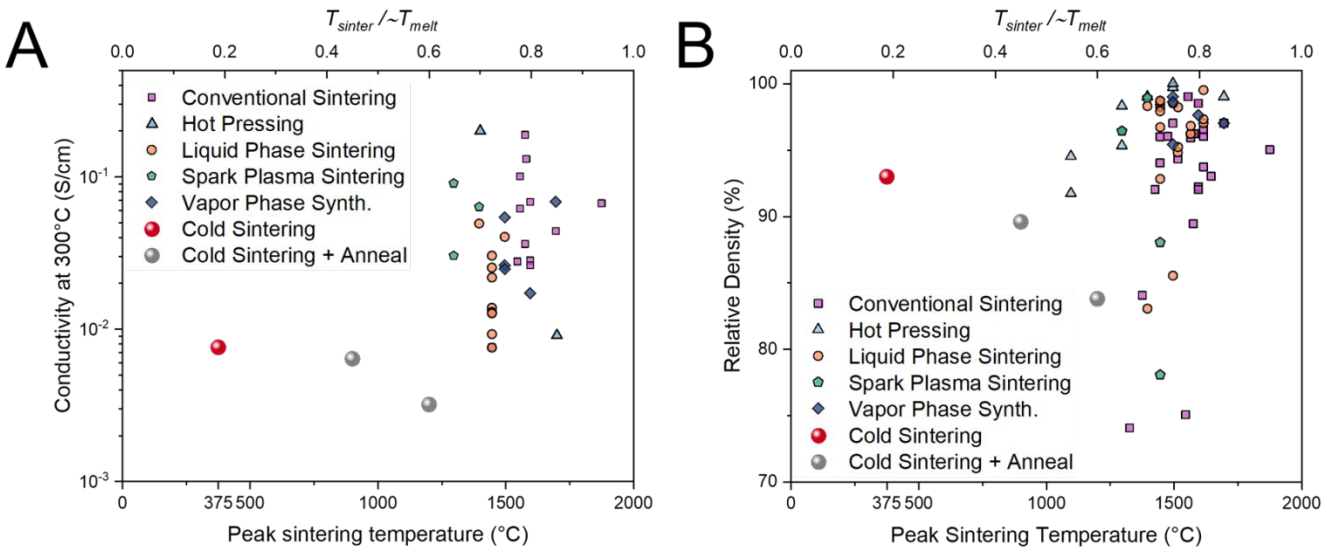

Figure 9 The ionic conductivity at 300°C (**A**) and relative density (**B**) are plotted as a function of peak sintering temperature for this work and a representative selection of prior work. Peak sintering temperature is defined as the maximum temperature observed by the samples prior to electrical measurement. A secondary *x*-axis of normalized sintering temperature (T_s/T_m) is also provided. A complete reference list with associated data is given in the supporting information (**Table S4**).

5. Conclusions

The cold sintering process was applied to the β''-Al_2O_3 solid-state electrolyte at 375°C using pure NaOH as the transient solvent. Coupled with 360 MPa of uniaxial pressure and a dwell time of three hours, a relative density of 92.7% is achieved. The microstructure of the samples is dense and retains the powder grain size (ca. 1 to 5 μm). The conductivity at 300°C of the as-cold-sintered β''-Al_2O_3 is $7.6 * 10^{-3}$ $S.cm^{-1}$, which exceeds the often-cited threshold of 1 $mS.cm^{-1}$ for an electrochemical cell with a thin electrolyte membrane. Near room temperature, the conductivity is low ($3.4 * 10^{-3}$ $S.cm^{-1}$) and the activation energy is high (0.54 eV) relative to conventionally sintered β''-Al_2O_3.

The poor low temperature conductivity is traced to interactions with moisture forming carbonates in parallel with amorphous grain boundary regions, which can be reversed with an argon annealing step at 900°C or 1200°C. Consistent with prior work, the room temperature conductivity is increased (reaching $5.2 * 10^{-5}$ S.cm^{-1}) and the activation energy is decreased (reaching 0.38 eV) with annealing, while the conductivity at 300°C remains above 10^{-3} S.cm^{-1}. The renormalization of the SBA sintering temperature from 80% of T_m (conventional solid-state sintering) to 20% of T_m (this work) may present new opportunities for co-processing this historically refractory solid electrolyte with chemically reactive electrodes for next-generation sodium-ion based energy storage technologies.

6. Author Contributions

Zane Grady: Methodology, Investigation, Formal Analysis, Writing – original draft, Writing – review & editing, Arnaud Ndayishimiye: Investigation, Formal Analysis, Writing – review & editing, Clive A. Randall: Conceptualization, Supervision, Funding acquisition, Project administration, Writing – review & editing.

7. Conflict of Interest

The authors have no conflicts of interest to disclose.

8. Acknowledgements

The authors (CAR, ZG) would like to gratefully acknowledge the Pacific Northwest National Laboratory and Battelle Corporation for providing financial support (Contract no. 500819). The authors (CAR, AN) would also like to thank the Air Force Office of Scientific Research (FA9550-19-1- 0372) for financial support for FTIR characterization.

The authors also thank Dr. Andrey Poletayev, Dr. David Reed, and Dr. Xiaolin Li for insightful technical discussions. The authors would also like to acknowledge Dr. Jennifer Gray and Dr. Zhongming Fan for their aid in performing cryogenic TEM for this study. The authors would also like to thank the anonymous reviewers for helpful comments and insight.

9. References

[1] K. B. Hueso, M. Armand, and T. Rojo, "High temperature sodium batteries: status, challenges and future trends," *Energy Environ. Sci.*, vol. 6, pp. 734–749, 2013.

[2] O. Bohnke, S. Ronchetti, and D. Mazza, "Conductivity measurements on nasicon and nasicon-modified materials," *Solid State Ionics*, vol. 122, no. 1–4, pp. 127–136, 1999.

[3] R. O. Ansell, "The chemical and electrochemical stability of beta-alumina," *J. Mater. Sci.*, vol. 21, pp. 365–379, 1986.

[4] M. Bettman and C. R. Peters, "The crystal structure of $Na_2O{\cdot}MgO{\cdot}5Al_2O_3$ with reference to $Na_2O{\cdot}5Al_2O_3$ and other isotypal compounds," *J. Phys. Chem.*, vol. 73, no. 6, pp. 1774–1780, 1969.

[5] C. R. Peters, M. Bettman, J. W. Moore, and M. D. Glick, "Refinement of the structure of sodium β-alumina," *Acta Crystallogr. Sect. B Struct. Crystallogr. Cryst. Chem.*, vol. 27, no. 9, pp. 1826–1834, 1971.

[6] L. C. De Jonghe, "Grain boundaries and ionic conduction in sodium beta alumina," *J. Mater. Sci.*, vol. 14, no. 1, pp. 33–48, 1979.

[7] M. C. Bay *et al.*, "Impact of liquid phase formation on microstructure and conductivity of Li-stabilized Na-β″-alumina ceramics," *ACS Appl. Energy Mater.*, vol. 2, no. 1, pp. 687–

693, 2019.

[8] S. N. Heavens, “Structural transformation during sintering and annealing of beta alumina,” *J. Mater. Sci.*, vol. 19, no. 7, pp. 2223–2232, 1984.

[9] D.-D. Lee, J.-H. Kim, and Yoon-Ho Kim, “The relative stability of beta and beta" -phases in Na20-AI203 beta alumina,” *J. Mater. Sci.*, vol. 25, pp. 2897–2900, 1990.

[10] J. D. Hodge, “Kinetics of the β″-to-β Transformation in the System Na_2O-$A1_2O_3$,” *J. Am. Ceram. Soc.*, vol. 66, no. 3, pp. 166–169, 1983.

[11] M. C. Bay *et al.*, “Impact of sintering conditions and zirconia addition on flexural strength and ion conductivity of Na-β”-alumina ceramics,” *Mater. Today Commun.*, vol. 23, no. January, p. 101118, 2020.

[12] M. Balaish, J. C. Gonzalez-Rosillo, K. J. Kim, Y. Zhu, Z. D. Hood, and J. L. M. Rupp, “Processing thin but robust electrolytes for solid-state batteries,” *Nat. Energy*, vol. 6, no. 3, pp. 227–239, 2021.

[13] T. Famprikis, P. Canepa, J. A. Dawson, M. S. Islam, and C. Masquelier, “Fundamentals of inorganic solid-state electrolytes for batteries,” *Nat. Mater.*, 2019.

[14] R. C. De Vries and W. L. Roth, “Critical Evaluation of the Literature Data on Beta Alumina and Related Phases: I, Phase Equilibria and Characterization of Beta Alumina Phases,” *J. Am. Ceram. Soc.*, vol. 52, no. 7, pp. 364–369, 1969.

[15] J.-H. Park, K.-H. Kim, and S.-K. Lim, “Influence of stabilizers on Na-β’’-Al_2O_3 phase formation in Li_2O(MgO)-Na_2O-Al_2O_3 ternary systems,” *J. Mater. Sci.*, vol. 33, pp. 5671–5765, 1998.

[16] T. D. Sparks and L. Ghadbeigi, "Anisotropic properties of Na-β″-alumina + YSZ composite synthesized by vapor phase method," *J. Mater. Res.*, vol. 33, no. 1, pp. 81–89, 2018.

[17] D. H. Lee, S. T. Lee, J. S. Kim, and S. K. Lim, "Analysis of properties of partially stabilized zirconia-doped Na^+-beta-alumina prepared by calcining-cum-sintering process," *Mater. Res. Bull.*, vol. 96, pp. 143–148, 2017.

[18] X. Wei, Y. Cao, L. Lu, H. Yang, and X. Shen, "Synthesis and characterization of titanium doped sodium beta″-alumina," *J. Alloys Compd.*, vol. 509, no. 21, pp. 6222–6226, 2011.

[19] H. A. Moghadam and M. H. Paydar, "Low-temperature sintering of sodium beta alumina ceramics using nanosized SnO_2 sintering aid," *Process. Appl. Ceram.*, vol. 14, no. 1, pp. 56–62, 2020.

[20] C. Chen, H. Katsui, and T. Goto, "Synthesis of sodium beta alumina films by heat treatment of sodium aluminum oxides," *J. Wuhan Univ. Technol. Mater. Sci. Ed.*, vol. 31, no. 1, pp. 6–10, 2016.

[21] A. V. Virkar, G. J. Tennenhouse, and R. S. Gordon, "Hot Pressing of Li_2O-Stabilized Beta''-Alumina," *J. Am. Ceram. Soc.*, vol. 57, no. 11, p. 508, 1974.

[22] A. Kishimoto, K. Shimokawa, and S. J. Jung, "Effect of sodium content on the mechanical and electrical properties of preferentially oriented Naβ-alumina ceramics," *J. Mater. Sci. Lett.*, vol. 22, no. 15, pp. 1083–1085, 2003.

[23] P. Vincenzini, A. Bellosi, and G. N. Babini, "The Influence of Powder Characteristics on the Vacuum Hot Pressing of Sodium Beta-Aluminas," *Mater. Chem.*, vol. 3, pp. 129–156,

1978.

[24] K. Li, Y. Yang, X. Zhang, and S. Liang, “Highly oriented β″-alumina ceramics with excellent ionic conductivity and mechanical performance obtained by spark plasma sintering technique,” *J. Mater. Sci.*, vol. 55, no. 20, pp. 8435–8443, 2020.

[25] S. Liang, Y. Yang, K. Li, and X. Zhang, “A study on the preparation of oriented beta“-alumina ceramics using rod/flake-like boehmite as precursors and their properties,” *J. Eur. Ceram. Soc.*, vol. 40, no. 12, pp. 4047–4055, 2020.

[26] K. Koganei, T. Oyama, M. Inada, N. Enomoto, and K. Hayashi, “C-axis oriented β ″ -alumina ceramics with anisotropic ionic conductivity prepared by spark plasma sintering,” *Solid State Ionics*, vol. 267, pp. 22–26, 2014.

[27] R. Subasri, T. Mathews, O. M. Sreedharan, and V. S. Raghunathan, “Microwave processing of sodium beta alumina,” *Solid State Ionics*, vol. 158, no. 1–2, pp. 199–204, 2003.

[28] C. Mortalò *et al.*, “Microwave assisted sintering of Na-β’’-Al_2O_3 in single mode cavities: Insights in the use of 2450 MHz frequency and preliminary experiments at 5800 MHz,” *Ceram. Int.*, vol. 46, no. 18, pp. 28767–28777, 2020.

[29] J. Guo *et al.*, “Cold Sintering: A Paradigm Shift for Processing and Integration of Ceramics,” *Angew. Chemie - Int. Ed.*, vol. 55, no. 38, pp. 11457–11461, 2016.

[30] M. Y. Sengul, C. A. Randall, and A. C. T. Van Duin, “ReaxFF Molecular Dynamics Study on the Influence of Temperature on Adsorption, Desorption, and Decomposition at the Acetic Acid/Water/ZnO(1010) Interface Enabling Cold Sintering,” *ACS Appl. Mater.*

Interfaces, vol. 10, no. 43, pp. 37717–37724, 2018.

[31] S. Lowum, R. Floyd, and J.-P. Maria, "Hydroflux-assisted densification: applying flux crystal growth techniques to cold sintering," *J. Mater. Sci.*, 2020.

[32] S. Grasso *et al.*, "A review of cold sintering processes," *Adv. Appl. Ceram.*, vol. 0, no. 0, pp. 1–29, 2020.

[33] A. Ndayishimiye *et al.*, "Comparing hydrothermal sintering and cold sintering process: Mechanisms, microstructure, kinetics and chemistry," *J. Eur. Ceram. Soc.*, vol. 40, no. 4, pp. 1312–1324, 2020.

[34] S. Uhlenbruck *et al.*, "Cathode-electrolyte material interactions during manufacturing of inorganic solid-state lithium batteries," *J. Electroceramics*, vol. 38, no. 2–4, pp. 197–206, 2017.

[35] Z. Grady *et al.*, "Cold Sintering for High-Temperature Electrochemical Applications," *Electrochem. Soc. Interface*, vol. 29, no. 4, pp. 59–65, 2020.

[36] J.-H. Seo *et al.*, "Cold sintering, enabling a route to co-sinter an all-solid-state lithium-ion battery," *Jpn. J. Appl. Phys.*, 2021.

[37] T. Ibn-Mohammed *et al.*, "Decarbonising ceramic manufacturing: A techno-economic analysis of energy efficient sintering technologies in the functional materials sector," *J. Eur. Ceram. Soc.*, vol. 39, no. 16, pp. 5213–5235, Dec. 2019.

[38] Z. M. Grady, K. Tsuji, A. Ndayishimiye, J. Hwan-Seo, and C. A. Randall, "Densification of a Solid-State NASICON Sodium-Ion Electrolyte Below 400 °C by Cold Sintering With a Fused Hydroxide Solvent," *ACS Appl. Energy Mater.*, vol. 3, no. 5, pp. 4356–4366,

2020.

[39] K. Tsuji *et al.*, "Single Step Densification of High Permittivity $BaTiO_3$ at 300 ^oC," *J. Eur. Ceram. Soc.*, 2019.

[40] S. Lowum, J. Maria, and R. D. F. Jr, "Cold sintering of magnetic $BaFe_{12}O_{19}$ and other ferrites at 300 ° C," *J. Mater. Sci.*, 2021.

[41] J.-H. Seo *et al.*, "Broad temperature dependence, high conductivity, and structure-property relations of cold sintering of LLZO-based composite electrolytes," *J. Eur. Ceram. Soc.*, vol. 40, no. June, pp. 6241–6248, 2020.

[42] W. Lee *et al.*, "Ceramic–Salt Composite Electrolytes from Cold Sintering," *Adv. Funct. Mater.*, vol. 1807872, p. 1807872, 2019.

[43] T. Zaengle *et al.*, "Single step densification of nanocrystalline CeO_2 by the cold sintering process," *J. Am. Ceram. Soc.*, vol. 1, no. 814, pp. 0–3, 2020.

[44] J. P. Gratier, D. K. Dysthe, and F. Renard, *The Role of Pressure Solution Creep in the Ductility of the Earth's Upper Crust*, vol. 54. Elsevier Inc., 2013.

[45] X. Zhang, C. J. Spiers, and C. J. Peach, "Compaction creep of wet granular calcite by pressure solution at 28°C to 150°C," *J. Geophys. Res. Solid Earth*, vol. 115, no. 9, pp. 1–18, Sep. 2010.

[46] S. Bell, T. Steinberg, and G. Will, "Corrosion mechanisms in molten salt thermal energy storage for concentrating solar power," *Renew. Sustain. Energy Rev.*, vol. 114, no. November 2018, p. 109328, 2019.

[47] S. N. Heavens, "Surface layers in polycrystalline sodium beta-alumina," *J. Mater. Sci.*,

vol. 17, no. 4, pp. 965–969, 1982.

[48] B. Dunn, "Effect of Air Exposure on the Resistivity of Sodium Beta and Beta'' Aluminas," *J. Am. Ceram. Soc.*, vol. 64, no. 3, pp. 125–128, 1981.

[49] D. Reed *et al.*, "Wetting of sodium on β″-Al_2O_3/YSZ composites for low temperature planar sodium-metal halide batteries," *J. Power Sources*, vol. 227, pp. 94–100, 2013.

[50] N. J. Dudney, J. B. Bates, and J. C. Wang, "Hydration of lithium β-alumina," *J. Chem. Phys.*, vol. 77, no. 10, pp. 4857–4869, 1982.

[51] N. Bonanos, B. C. . Steele, and E. P. Butler, "Applications of Impedance Spectroscopy," in *Impedance Spectroscopy: Theory, Experiment, and Applications*, 2nd ed., E. Barsoukov and J. R. Macdonald, Eds. Hoboken, NJ, USA: John Wiley & Sons, Ltd, 2005, pp. 205–264.

[52] B. J. T. S. Irvine, D. C. Sinclair, and A. R. West, "Electroceramics Characterisation by impedance sepctroscopy," *Adv. Mater.*, vol. 2, no. 3, pp. 132–138, 1990.

[53] S. Havriliak and S. Negami, "A complex plane representation of dielectric and mechanical relaxation processes in some polymers," *Polymer (Guildf).*, vol. 8, no. C, pp. 161–210, 1967.

[54] C. Grosse, "A program for the fitting of Debye, Cole-Cole, Cole-Davidson, and Havriliak-Negami dispersions to dielectric data," *J. Colloid Interface Sci.*, vol. 419, pp. 102–106, 2014.

[55] C. León, M. Lucía, and J. Santamaría, "Correlated ion hopping in single-crystal yttria-stabilized zirconia," *Phys. Rev. B - Condens. Matter Mater. Phys.*, vol. 55, no. 2, pp. 882–

887, 1997.

[56] P. Vadhva *et al.*, "Electrochemical Impedance Spectroscopy for All-Solid-State Batteries: Theory, Methods and Future Outlook," *ChemElectroChem*, vol. 8, no. 11. pp. 1930–1947, 2021.

[57] C. Zhu, Y. Hong, and P. Huang, "Synthesis and characterization of NiO doped beta-Al_2O_3solid electrolyte," *J. Alloys Compd.*, vol. 688, pp. 746–751, 2016.

[58] J. H. Kim *et al.*, "Electrical characterization of polycrystalline sodium β″- alumina: Revisited and resolved," *Solid State Ionics*, vol. 264, pp. 22–35, 2014.

[59] B. Wang and A. N. Cormack, "Molecular dynamics simulations of Mg-doped beta″-alumina with potential models fitted for accurate structural response to thermal vibrations," *Solid State Ionics*, vol. 263, pp. 9–14, 2014.

[60] M. Alden, J. O. Thomas, and P. Davies, "The Effect opf Quenching on The Na+ Ion Distribution in Na+ Beta''-Alumina," *Solid State Ionics*, vol. 18–19, pp. 694–698, 1986.

[61] S. Barison, S. Fasolin, C. Mortalò, S. Boldrini, and M. Fabrizio, "Effect of precursors on β-alumina electrolyte preparation," *J. Eur. Ceram. Soc.*, vol. 35, no. 7, pp. 2099–2107, 2015.

[62] Y. Sheng, P. Sarkar, and P. S. Nicholson, "The mechanical and electrical properties of ZrO_2-Na β″-Al_2O_3 composites," *J. Mater. Sci.*, vol. 23, no. 3, pp. 958–967, 1988.

[63] S. T. Lee, D. H. Lee, S. M. Lee, S. S. Han, S. H. Lee, and S. K. Lim, "Effects of calcium impurity on phase relationship, ionic conductivity and microstructure of Na+-β/β″-alumina solid electrolyte," *Bull. Mater. Sci.*, vol. 39, no. 3, pp. 729–735, 2016.

[64] S. T. Lee, D. H. Lee, J. S. Kim, and S. K. Lim, "Influence of Fe and Ti addition on properties of Na+-β/β″-alumina solid electrolytes," *Met. Mater. Int.*, vol. 23, no. 2, pp. 246–253, 2017.

[65] M. Demartin, C. Hérard, C. Carry, and J. Lemaître, "Dedensification and anomalous grain growth during sintering of undoped barium titanate," *J. Am. Ceram. Soc.*, vol. 80, no. 5, pp. 1079–1084, 1997.

[66] P. Duran, J. Tartaj, and C. Moure, "Sintering behaviour and microstructural evolution of agglomerated spherical particles of high-purity barium titanate," *Ceram. Int.*, vol. 29, no. 4, pp. 419–425, 2003.

[67] C. Hérard, A. Faivre, and J. Lemaître, "Surface decontamination treatments of undoped $BaTiO_3$-part I: Powder and green body properties," *J. Eur. Ceram. Soc.*, vol. 15, no. 2, pp. 135–143, 1995.

[68] M. Nagai, T. Kushida, and T. Nishino, "Effect of water vapor on the conductivity of porous Na β/β″-Al_2O_3 ceramics," *Solid State Ionics*, vol. 40–41, no. PART 1, pp. 107–110, 1990.

[69] K. Buijs and C. J. H. Schutte, "An infra-red study of the hydrates of sodium carbonate," *Spectrochim. Acta*, vol. 17, no. 9–10, pp. 917–920, 1961.

[70] A. Vázquez, T. López, R. Gómez, Bokhimi, A. Morales, and O. Novaro, "X-Ray Diffraction, FTIR, and NMR Characterization of Sol-Gel Alumina Doped with Lanthanum and Cerium," *J. Solid State Chem.*, vol. 128, no. 2, pp. 161–168, 1997.

[71] J. B. Bates, D. Dohy, and R. L. Anderson, "Reaction of polycrystalline Na β″ -alumina

with CO_2 and H_2O and the formation of hydroxyl groups," *J. Mater. Sci.*, vol. 20, no. 9, pp. 3219–3229, 1985.

[72] A. Hooper, "A study of the electrical properties of single-crystal and polycrystalline β-alumina using complex plane analysis," *J. Phys. D. Appl. Phys.*, vol. 10, no. 11, pp. 1487–1496, 1977.

[73] S. J. Shan, L. P. Yang, X. M. Liu, X. L. Wei, H. Yang, and X. D. Shen, "Preparation and characterization of TiO_2 doped and MgO stabilized Na-β″-Al_2O_3 electrolyte via a citrate sol-gel method," *J. Alloys Compd.*, vol. 563, pp. 176–179, 2013.

[74] A. Mali and A. Petric, "Synthesis of sodium β'-alumina powder by sol-gel combustion," *J. Eur. Ceram. Soc.*, vol. 32, no. 6, pp. 1229–1234, 2012.

[75] A. C. Sutorik, S. S. Neo, D. R. Treadwell, and R. M. Laine, "Synthesis of Ultrafine Beta-Alumina Powders via Flame Spray Pyrolysis of Polymeric Precursors," *J. Am. Ceram. Soc.*, vol. 81, no. 6, pp. 1477–1486, 1998.

[76] A. Imai and M. Harata, "Ionic conduction of impurity-doped β-alumina ceramics," *Jpn. J. Appl. Phys.*, vol. 11, no. 2, pp. 180–185, 1972.

[77] T. J. Whalen, G. J. Tennenhouse, and C. Meyer, "Relation of Properties to Microstructure in a B"-Alumina Ceramic," *J. Am. Ceram. Soc.*, vol. 57, pp. 497–498, 1974.

[78] H. Li *et al.*, "Performance of Nano-3YSZ toughened β''-Alumina solid electrolyte prepared by EDTA-Zr(IV)/Y(III) complex as surface modifier," *J. Alloys Compd.*, vol. 817, p. 152717, 2020.

[79] X. Lu, G. Li, J. Y. Kim, K. D. Meinhardt, and V. L. Sprenkle, "Enhanced sintering of βa″-

Al_2O_3/YSZ with the sintering aids of TiO_2 and MnO_2," *J. Power Sources*, vol. 295, pp. 167–174, 2015.

[80] L. B. Caliman, R. Bouchet, D. Gouvea, P. Soudant, and M. C. Steil, "Flash sintering of ionic conductors: The need of a reversible electrochemical reaction," *J. Eur. Ceram. Soc.*, vol. 36, no. 5, pp. 1253–1260, 2016.

[81] C. Zhang, L. Zhang, P. Zheng, and X. Zhang, "Synthesis of magnesium-beta-alumina composite electrolytes via a vapour phase method," *Ceram. Int.*, vol. 46, no. 8, pp. 12232–12237, 2020.